

# Implementation and evaluation of a 3D one-step late reconstruction algorithm for 3D positron emission tomography brain studies using median root prior

V. Bettinardi<sup>1</sup>, E. Pagani<sup>1</sup>, M.C. Gilardi<sup>1</sup>, S. Alenius<sup>2</sup>, K. Thielemans<sup>4</sup>, M. Teras<sup>3</sup>, F. Fazio<sup>1</sup>

<sup>1</sup> Department of Nuclear Medicine, Scientific Institute H.S.Raffaele, University of Milano-Bicocca, INB-CNR, Via Olgettina 60, 20132 Milan, Italy

<sup>2</sup> Tampere University of Technology, Signal Proc. Lab, Finland

<sup>3</sup> Turku PET Center, Finland

<sup>4</sup> Imaging Research Solutions Ltd, Hammersmith Hospital, UK

Received 27 April and in revised form 17 August 2001 / Published online: 1 November 2001

© Springer-Verlag 2001

**Abstract.** A fully three-dimensional (3D) one-step late (OSL), maximum a posteriori (MAP) reconstruction algorithm based on the median root prior (MRP) was implemented and evaluated for the reconstruction of 3D positron emission tomography (PET) studies. The algorithm uses the ordered subsets (OS) scheme for convergence acceleration and data update during iterations. The algorithm was implemented using the software package developed within the EU project PARAPET ([www.brunel.ac.uk/~masrppet](http://www.brunel.ac.uk/~masrppet)). The MRP algorithm was evaluated using experimental phantom and real 3D PET brain studies. Various experimental set-ups in terms of activity distribution and counting statistics were considered. The performance of the algorithm was assessed by calculating figures of merit such as: contrast, coefficient of variation, activity ratio between two regions and full width at half of maximum for resolution measurements. The performance of MRP was compared with that of 3D ordered subsets-expectation maximisation (OSEM) and 3D re-projection (3DRP) algorithms. In all the experimental situations considered, MRP showed: (1) convergence to a stable solution, (2) effectiveness in noise reduction, particularly for low statistics data, (3) good preservation of spatial details. Compared with the OSEM and 3DRP algorithms, MRP provides comparable or better results depending on the parameters used for the reconstruction of the images.

**Keywords:** Iterative reconstruction algorithm – 3D – Positron emission tomography

V. Bettinardi (✉)

Department of Nuclear Medicine, Scientific Institute H.S.Raffaele, University of Milano-Bicocca, INB-CNR, Via Olgettina 60, 20132 Milan, Italy

e-mail: [vale@mednuc.hsr.it](mailto:vale@mednuc.hsr.it)

Tel.: +39-02-26432716, Fax: +39-02-26415202

**Eur J Nucl Med (2002) 29:7–18**

DOI 10.1007/s002590100651

## Introduction

Two main classes of image reconstruction algorithm are used in positron emission tomography (PET): analytical and iterative methods. Analytical methods are the most widely used since they are fast and linear. However, the reconstructed images suffer from streak artefacts due to the filtering employed. Iterative methods have been demonstrated to generate images of good quality with the advantage of being less sensitive to artefacts related to the poor statistics of the acquired data. Furthermore, iterative techniques are more “flexible” with respect to analytical methods, allowing the intrinsic random nature of the emission and detection processes, as well as the characteristics of each specific PET scanner, to be incorporated in the reconstruction scheme. On the other hand, the computational cost of the iterative algorithms is very high, especially when data acquired in three-dimensional (3D) mode have to be reconstructed. Nevertheless, the continuous development of new and more powerful processors and the use of parallel architectures mean that iterative techniques are becoming more feasible even for clinical applications. In fact, iterative methods are now available in the application software of commercial PET systems at least for the reconstruction of PET data acquired or re-binned into two-dimensional (2D) mode.

One of the most investigated methods for iterative image reconstruction in PET is the maximum likelihood-expectation maximisation (ML-EM) technique [1, 2], where the PET reconstruction problem is solved as a statistical estimation, the unknown parameters being the local isotope concentrations in each voxel of the image. Maximisation of the likelihood function is achieved by iteratively

sing the likelihood function with respect to the unknown parameters yields the parameters with which the data are consistent. Unfortunately, the EM algorithm is extremely computer intensive and its convergence is very slow. Several techniques have been developed in order to accelerate the convergence in EM [3]. One of the most successful methods has been proposed by Hudson and Larkin [4] as the ordered subsets-expectation maximisation (OSEM) algorithm. OSEM maintains the same scheme as EM with the difference that the data are processed in subsets within each iteration. In the OSEM reconstruction scheme, the image is updated more frequently than in EM (every time each subset of projections is used), and this accelerates the convergence by a factor nearly proportional to the number of subsets used. Another common problem of the EM-based algorithms is the increase in the noise in the reconstructed images as the number of iterations proceeds. This is due to the ill-posedness nature of the reconstruction problem, where small changes in the measured data may cause large changes in the estimated image [5]. In order to avoid increase in the noise, the iterations can be stopped before convergence [6]. This approach suffers from a noise/bias trade-off: if the convergence is reached, the image is too noisy [7]; if a small number of iterations is used, the image is less noisy, but, quantitatively, it is biased towards the initial starting image [8].

In order to avoid these problems, several regularisation methods have been developed. One such interesting method was proposed by Green [9]. This is the one-step late (OSL) maximum a posteriori (MAP) method, which introduces a penalty function (PF) with the aim of regularising the solution as the iterations proceed, allowing the convergence of the algorithm to the maximum of the penalised likelihood. Depending on the characteristics of the PF used, some features in the reconstructed images can in fact be penalised or not. The choice of the PF is generally based on assumptions about the characteristics of the image to be reconstructed. When the assumption is that the true image distribution is smooth, a quadratic PF can be used [10]. The effect of a quadratic PF is to set a penalty on the difference between neighbouring pixels, in order to suppress noise and force the solution towards a smooth image. As a side-effect of this, edges and transitions between different activity levels in the image are blurred. On the other hand, emission PET images can be spatially complex, with non-smooth regions and with the presence of sharp transitions between different tissues (e.g. grey and white matter in brain studies, lung and soft tissue in whole-body studies). In these cases the PF can be further tailored with specific extra threshold parameters in order to be less effective in penalising sharp transitions and step edges [9, 10] and to prevent excessive blurring [11]. The optimisation of this PF is difficult owing to the fact that the true edge height is generally unknown. Furthermore, detection of a low transition of the activity levels is most important because it could represent a small quantitative difference between concentrations in adjacent tissue areas.

If the threshold used is properly set, high edges are not too blurred, but small changes in activity levels will still be penalised, thus degrading the sensitivity in distinguishing abnormal changes in tracer activity [12].

Recently Alenius et al. have proposed the use of the median root prior (MRP) [12, 13] as the PF. In the MRP PF the penalty is set for a pixel against the local median: the penalty is set only if within the local pixel neighbourhoods, the image is non-monotonic. No other constraints are used. MRP PF has advantages in that it does not require a priori information and it is not specifically dependent on image quantitative aspects (neither edge height nor image noise amplitude) [12]. The algorithm has been successfully evaluated with 2D PET and single-photon emission tomography (SPET) data, showing interesting properties in terms of both noise reduction and quantitative accuracy [12, 13, 14].

In this work, we implemented a 3D version of the MRP reconstruction algorithm. The algorithm was implemented using the reconstruction package developed within the EU project PARAPET ([www.brunel.ac.uk/~masrppet](http://www.brunel.ac.uk/~masrppet)) [15]. It was evaluated using experimental phantom and real 3D PET brain studies. The performance of the MRP algorithm was compared with 3D OSEM and 3D reprojection (3DRP) [16], which represent two of the most investigated fully 3D PET iterative and analytical reconstruction algorithms, respectively.

## Materials and methods

### Algorithm implementation

Notation is as follows:

$\lambda^n$	Image at the $n$ th iteration
$b, b'$	Voxel index, $1 \leq b \leq B$
$d$	Detector pair index, $1 \leq d \leq D$
$p_{db}$	Probability matrix: probability that annihilation photon pairs emitted from voxel $b$ are detected in the detector pair $d$
$n_d$	Measured counts at detector pair $d$
$\lambda_d$	Mean counts at detector pair $d$
$\lambda_b$	Mean counts at voxel $b$
LOR	Line of response: tube which connects a pair of opposite detectors in coincidence

The OSEM algorithm is:

$$\lambda_b^{n+1} = \frac{\lambda_b^n}{\sum_{d \in D_k} p_{db}} \sum_{d \in D_k} \frac{n_d p_{db}}{\sum_{b' \in B} \lambda_{b'}^n p_{db'}} \quad (1)$$

where  $D_k$  represents a partition of the projection space into  $m$  subsets,  $n = 0, 1, 2, \dots$  is the sub-iteration number and  $k = n \bmod m$ . A cycle of  $m$  sub-iterations constitutes a complete iteration.

Consider the OSL algorithm in its general form:

$$\lambda_b^{n+1} = \frac{\lambda_b^n}{\sum_{d \in D} p_{db} + \beta \frac{\partial}{\partial \lambda_b} U(\lambda, b) |_{\lambda=\lambda^n}} \sum_{d \in D} \frac{n_d p_{db}}{\sum_{b' \in B} \lambda_{b'}^n p_{db'}} \quad (2)$$

where  $U(\lambda, b)$  is a potential function while  $\beta$  is the weight factor.

The MRP algorithm can be formulated using the median as a penalty reference:

$$\beta \frac{\partial}{\partial \lambda_b} U(\lambda, b) |_{\lambda=\lambda^n} = \beta \frac{\lambda_b^n - M_b(\lambda^n)}{M_b(\lambda^n)} \quad (3)$$

where  $M_b$  is the median in a  $3 \times 3 \times 3$  mask width of neighbourhood voxels centered at voxel  $b$ . The penalty is set if the voxel  $\lambda_b$  is different from  $M_b$ .

Another important factor in the implementation of the iterative algorithm is related to the probability matrix (PM) used in the reconstruction scheme. The PM ( $p_{db}$ ) can be decomposed into several sub-factors which account for physical effects:

$$p_{db} = \epsilon_d \rho_d p_{g\_db} \dots \quad (4)$$

where:  $\epsilon_d$  is the intrinsic efficiency of the detector pair  $d$ ;  $\rho_d$  is the probability that an event propagating in the LOR related to the detector pair  $d$  will survive the attenuation of the medium; and  $p_{g\_db}$  is the probability that an emission from voxel  $b$  will be detected in the detector pair  $d$  with respect to geometric factors only. Other possible factors to be considered in the PM are: positron range, non-collinearity effects of the annihilation photons, randoms and scatter corrections. In our implementation, data are pre-corrected for randoms, detector normalisation and scatter, while geometric and physical attenuation factors are included in the PM.

The algorithm was implemented using the PARAPET software. This is an object-oriented software library (written in C++) [15], which provides general classes for image and sinogram manipulation, forward- and back-projection routines and some reconstruction algorithms, including the basic 3D OSEM algorithm. In this work, the parallel version of the code was used, which is based on a master-slave architecture. For details on the parallel implementation, see Jacobson et al. [17]. The computing platform used for this work was a Parsytec (Aachen, Germany) computer (CC-12) with operating system AIX 4.2.1 consisting of 12 nodes, each equipped with a 133-MHz power PC 604 CPU and 128 MB of RAM.

## PET scanner

The PET tomograph used in this study was the GE-Advance scanner (General Electric Medical System, Milwaukee, Wis.). The system consists in 12,096 bismuth germanate crystals organised in 18 rings. The crystals have a dimension of 4.0 mm transversally, 8.1 mm axially and 30 mm radially. A detection unit (block) consists of  $6 \times 6$  crystals, coupled to two double photomultipliers. The 18 crystal rings allow 35 2D images to be obtained, spaced by 4.25 mm, covering an axial field of view (FOV) of 15.2 cm. The system has tungsten septa 1 mm thick and 12 cm long. The septa, which define the image planes in the 2D scanning mode, can be automatically retracted to allow radiation detection in the 3D scanning mode. Transmission (TR) data can be recorded using a pair of germanium-68 pin sources, which can be automatically positioned in the scanner FOV and rotated around the longitudinal axis of the scanner.

## Phantom studies

In all phantom studies a TR scan of 10 min was acquired for use in attenuation correction.

*Mixed cold-hot-line phantom (MIX).* The MIX phantom consists of a 20-cm cylindrical phantom (length = 20 cm) filled with a uniform solution of water and fluorine-18 [ $^{18}\text{F}$ ]. Several inserts were positioned in the phantom:

1. A Jaszczak (JZA) phantom. The JZA consists of six sectors of cold cylindrical rods. The diameters of the cold rods are 12.7, 11.1, 9.5, 8.4, 6.4 and 4.5 mm. The JZA insert covers the lower half of the 20-cm length of the MIX phantom.
2. Six hot spheres (containing a radioactive solution of water and  $^{18}\text{F}$ ) with diameters of 2.3, 1.3, 1.3, 1.1, 0.8 and 0.8 cm. The radioactivity concentration ratio between hot spheres and background was 7.6.
3. Two line sources (inner diameter = 1 mm, length = 5 cm). One line source was positioned in the centre of the cylinder while the second was 8 cm off axis.

The MIX phantom was positioned in the centre of the scanner FOV and two emission (EM) scans of 200 Mcounts (EM1) and 30 Mcounts (EM2) were performed.

*3D Hoffman brain phantom (HB).* The 3D HB phantom was filled with a homogeneous solution of water and  $^{18}\text{F}$  (22.6 MBq in the phantom). An emission acquisition, EM1 (200 Mcounts), was performed, representative of clinical 3D PET brain studies of regional glucose metabolism with [ $^{18}\text{F}$ ]fluorodeoxyglucose ( $^{18}\text{F}$ -FDG).

*Striatal phantom (ST).* The ST phantom was filled with homogeneous solutions of water and  $^{18}\text{F}$ : 43.4 kBq/cc and 11.3 kBq/cc in the compartments simulating the "striata" (caudate and putamen) and the surrounding background, respectively. An acquisition: EM1 (33 Mcounts) was performed simulating a 3D PET brain study with [ $^{18}\text{F}$ ]fluoroethylspiperone ( $^{18}\text{F}$ -FESP).

## Clinical studies

An  $^{18}\text{F}$ -FDG and an  $^{18}\text{F}$ -FESP PET brain study were considered to evaluate the performances of the algorithms with real data. In both cases, a 3D 10-min EM scan was acquired 45 min after the tracer injection followed by a 2D (5-min) emission scan and by a post-injection TR scan (15 min). TR data were used for attenuation correction following the same data processing as for phantom studies (see next section).

## Reconstruction algorithms and reconstruction set-up

Phantom and clinical studies were reconstructed by OSEM, MRP and 3DRP.

Raw data were pre-corrected for randoms, arc correction, detector normalisation, scatter, dead time, and radioactivity decay.

All the studies were reconstructed on a 55-cm FOV using a  $281 \times 281$  image matrix (pixel size = 1.95 mm).

The following parameters were used for OSEM and MRP: subsets = 14, 3D median penalisation (only for MRP),  $\beta$  parameter = 0.0001/subset, 0.0003/subset, 0.0005/subset and 0.0009/subset. To avoid long notations, these MRP configurations will be identified in the text as MRP-b1, MRP-b3, MRP-b5 and MRP-b9, respectively. Few other parameter configurations were considered in the work, and they will be specifically described when needed. Geometrical factors ( $p_{g\_db}$ ) and attenuation factors ( $\rho_d$ ) were included in the reconstruction scheme. TR images were reconstructed using a 2D filtered back-projection algorithm and then segmented to eliminate the

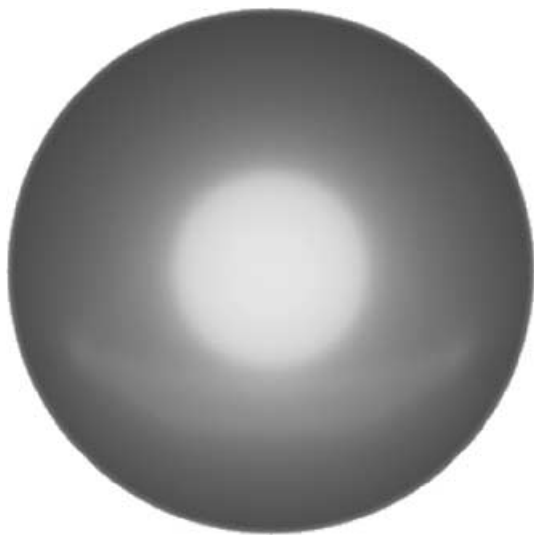


**Fig. 1.** Example of probability matrix (PM) used in OSEM and MRP algorithms. Geometric and attenuation effects are included in the PM

**Table 1.** Filters used for 3DRP reconstructions

3DRP	Colsher transaxial window	Cut-off	Colsher axial window	Cut-off
RR	Rectangular	0.5	Rectangular	0.5
HR	Hanning	0.5	Rectangular	0.5
HH	Hanning	0.5	Hanning	0.5

residual noise present in the TR reconstructed images [18]. The segmented TR images were then used to build the PM, which included geometric and attenuation effects (Fig. 1). Three reconstruction protocols were considered for 3DRP (Table 1). Condition 1 (RR) allows the best resolution to be maintained in the images, but usually with too high noise. Condition 2 (HR) represents a compromise in terms of noise reduction in the transaxial plane, while maintaining “good” spatial resolution in the axial direction. Condition 3 (HH) represents a typical set-up used in clinical applications with low statistics data. Attenuation correction in 3DRP was performed by forward-projection of the segmented TR images.

#### Data analysis

Data analysis was performed by calculating for each phantom and clinical study a figure of merit (FOM), based on the use of regions of interest (ROI).

#### MIX phantom

The MIX phantom was used to evaluate several FOMs simultaneously, such as:

- *Regions of uniform activity background.* Large ROIs were drawn in six slices of the MIX phantom in regions of uniform

activity background. Mean, standard deviation (SD) and coefficient of variation (CV) = (SD/mean) were calculated for each ROI.

- *Contrast on cold rods: JZA phantom region.* ROIs of the same diameter as the cold rods were drawn in each sector of the JZA phantom (with the exception of the smallest ones of 4.8 mm, which were hardly recognisable in the reconstructed images). Contrast ( $C = (ROI_{bckg} - ROI_{cold}) / ROI_{bckg}$ ) and CV (only for the background) were calculated for each sector of the phantom.
- *Activity ratio on hot spheres.* An ROI of the same diameter of the sphere was drawn in one slice (the most central) of each sphere. The activity ratio (AR) was then calculated between the activity concentration in the sphere and the activity concentration in the background.
- *Line sources: full width at half of maximum (FWHM).* FWHM was measured on a radial and a tangential profile drawn through the reconstruction of the two line sources. FWHM was calculated by linear interpolation between adjacent pixels at half of the maximum pixel value. Line sources were reconstructed as described in the *Reconstruction algorithms and reconstruction set-up* section in order to evaluate the performance of the algorithms as used for phantom and real data.

#### HB phantom

Circular ROIs with diameter of 5 mm were drawn over the “grey” and “white” matter regions on two representative central slices.

AR between “grey” and “white” matter regions was calculated. CV was calculated over “white” matter ROIs.

#### ST phantom

Circular ROIs with diameter of 4.5 mm were drawn over the “putamen”, the “caudate” and the surrounding background.

AR between “putamen” and background as well as the “caudate” and background were calculated, while CV was calculated only for the background activity.

#### Clinical studies

The same methods of analysis as were used for the HB and ST phantoms were used for the  $^{18}\text{F}$ -FDG and  $^{18}\text{F}$ -FESP PET brain studies, respectively.

## Results

### Phantom studies

#### MIX phantom

*Regions of uniform activity background.* Figure 2 shows CV values as a function of the number of iterations for the low statistics data (EM2=30 Mcounts). MRP showed a trend to converge to a stable solution for all the considered configurations. OSEM showed a typical increase in noise as the iterations proceeded. In order to achieve a noise level comparable to MRP, OSEM should be



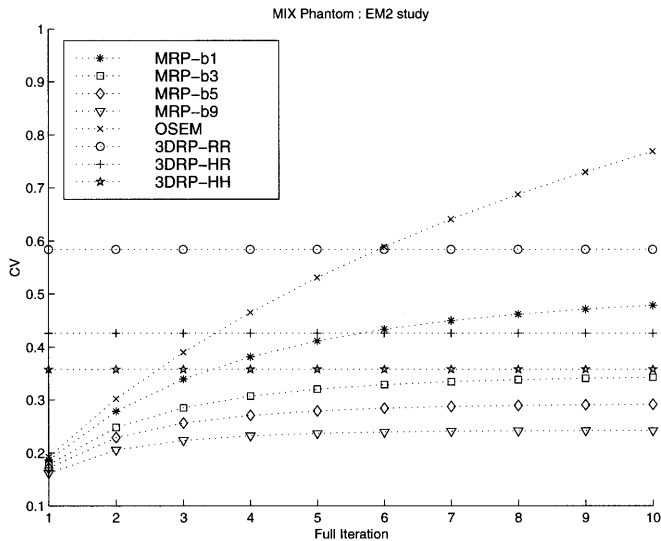


**Fig. 2.** MIX phantom (EM2=30 Mcounts). Coefficient of variation (CV) as a function of number of iterations for all reconstruction algorithms and reconstruction set-ups. 3DRP data are represented with a constant value over iterations only for easy comparison with OSEM and MRP algorithms

stopped after 2–3 complete iterations. 3DRP generally showed a higher CV than did MRP. Similar results were found for the high statistics study (EM1=200 Mcounts).

*Cold contrast on rods: JZA phantom region.* Figure 3 shows C values as a function of CV, for the cold rods of 12.7 mm (a) and 6.4 mm (b), in the case of low counting statistics (EM2=30 Mcounts). For the 12.7-mm lesion, 3DRP<sub>RR</sub> reached the highest C. OSEM reached a higher C (~13%) after 15 complete iterations than did MRP-b9 but with a higher noise level (~70%). OSEM, after 4–5 complete iterations, had lower C and higher noise than MRP after ~10 complete iterations. For the 6.4-mm rod sector, OSEM reached a comparable or higher C than MRP (b3–b9) even for a low number of complete iterations (4–5), while MRP had a generally lower CV. The performances of MRP degraded more rapidly, in terms of C, for the 6.4-mm lesion than for the 12.7-mm lesion using different  $\beta$  values. 3DRP had an intermediate behaviour in terms of C and CV in comparison with the iterative algorithms. Contrast calculated on the high statistics data showed results similar to those described above for the low statistics dataset study. In Fig. 4 the reconstructed images of the JZA phantom for the high statistics study (EM1) are shown. Image quality reflects the quantitative results described above. Some apparent artefacts (other than the cold rods) visible in the JZA images are due to the presence of the supports of all the hot spheres.

*Activity ratio on hot spheres.* The % error with respect to the true AR values for the 8-mm hot sphere in the low

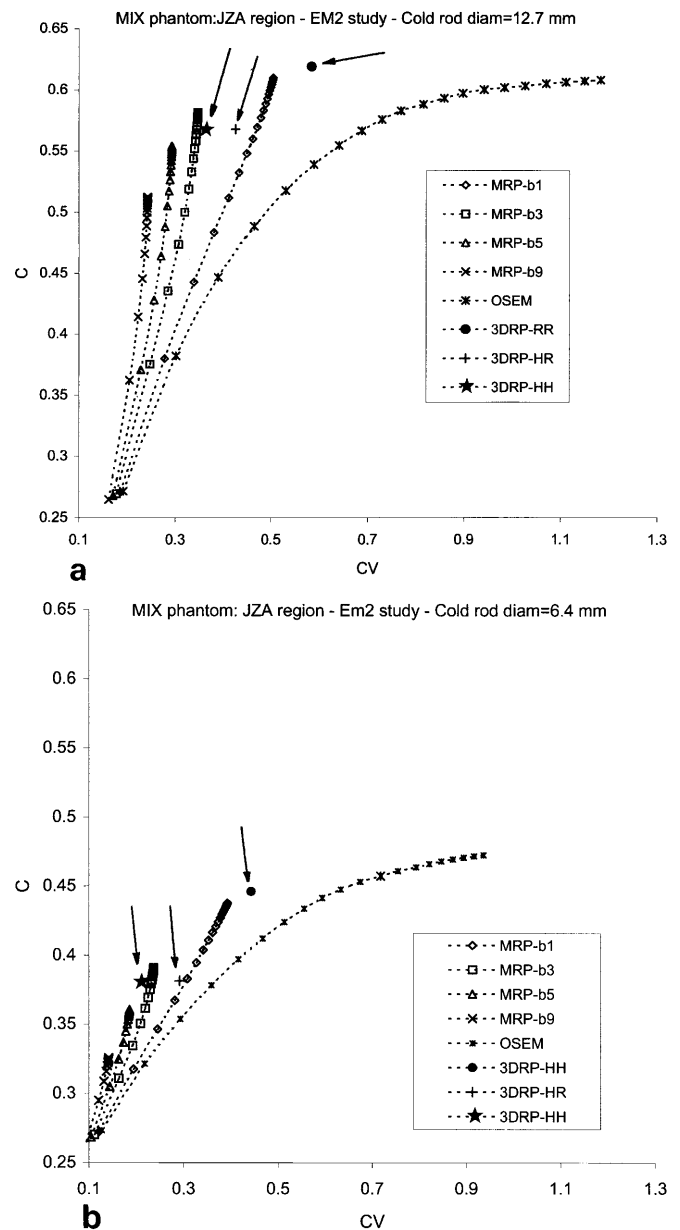


**Fig. 3a, b.** MIX phantom (EM2=30 Mcounts). JZA region. Contrast C as a function of CV: **a** 12.7-mm cold rods, **b** 6.4-mm cold rods. 3DRP values are indicated by arrows for easy identification

statistics study are shown in Fig. 5 as a function of CV. OSEM reached the lowest % error after ~10 complete iterations but also showed the highest noise level. At 2–3 complete iterations, OSEM had a % error comparable to MRP-b3 and MRP-b5 at convergence, but also with higher noise. 3DRP did not show optimal performance in terms of either % error or CV. Increasing the size of the spheres (so that they became larger in relation to the median filter mask) reduced the resolution effect on MRP and, as a general trend, MRP then performed better than OSEM. Similar results were found for the high statistics study.

**Fig. 4.** MIX phantom: JZA region (EM1 study). *Top row (from left to right):* 3DRP<sub>RR</sub>, 3DRP<sub>HR</sub>, 3DRP<sub>HH</sub>. *Middle row (from left to right):* OSEM after 10, 4 and 3 complete iterations. *Bottom row (from left to right):* MRP-b3, MRP-b5 and MRP-b9. All the MRP images were obtained after 10 complete iterations

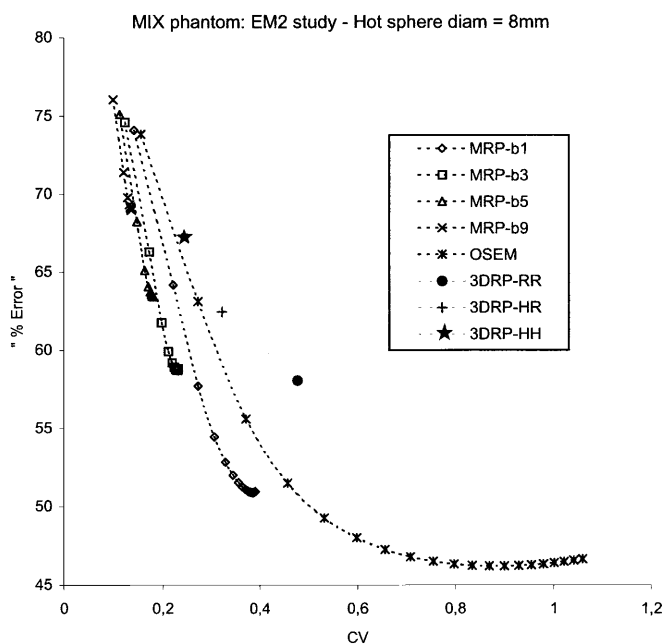
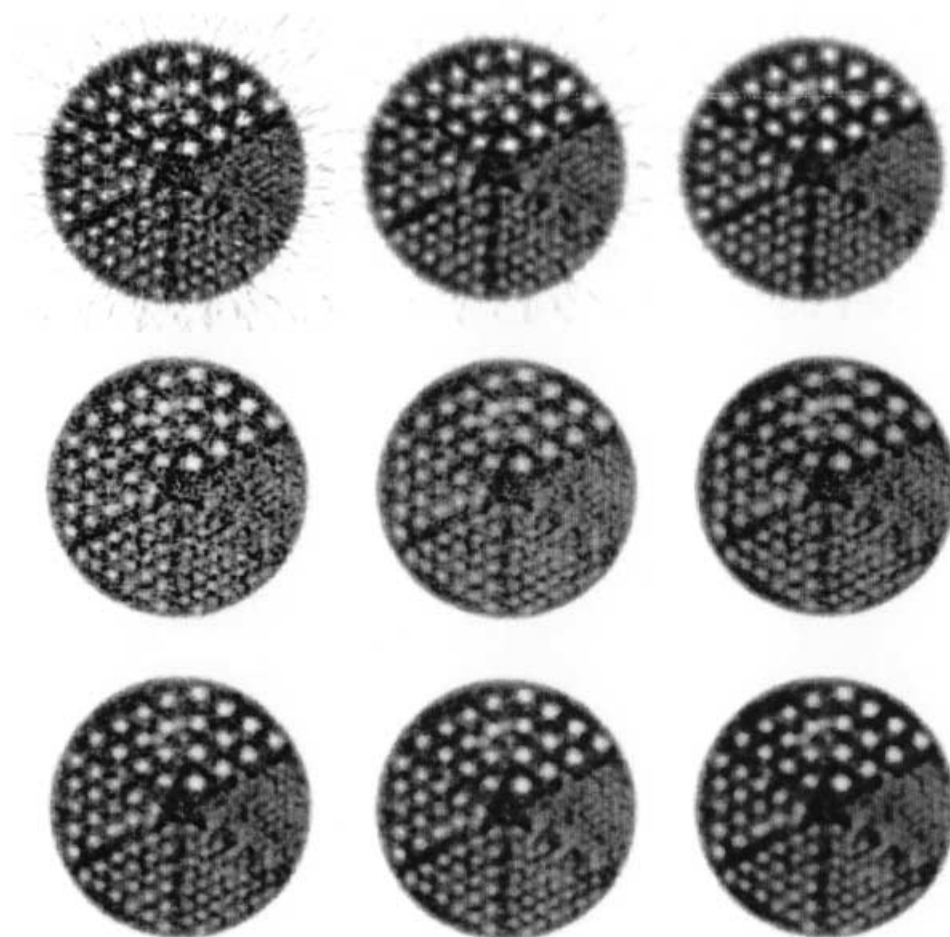


**Fig. 5.** MIX phantom: EM2 study. % error of the activity ratio AR between hot sphere (8 mm) and background in relation to the true AR value as a function of CV

**Table 2.** Resolution measurements. FWHM as measured for the line source in the MIX phantom. OSEM FWHM was measured after 4 and 10 complete iterations while MRP values were measured after 10 complete iterations

Algorithm	Radial FWHM (mm) On-axis	Tangential FWHM (mm) On-axis	Radial FWHM (mm) 8 cm off-axis	Tangential FWHM (mm) 8 cm off-axis
3DRP – RR	5.4	5.3	5.8	5.3
3DRP – HR	6.4	6.5	7.0	6.5
3DRP – HH	6.4	6.5	7.0	6.6
OSEM – 4 full it.	4.3	4.5	5.1	4.6
OSEM – 10 full it.	4.2	4.4	4.9	4.6
MRP-b3	5.3	4.8	5.5	5.3
MRP-b5	5.6	5.2	5.7	5.6
MRP-b9	5.8	5.9	6.0	5.9

*Line sources: full width at half of maximum.* FWHMs calculated for the line sources (on-axis and 8 cm off-axis) are reported in Table 2. In terms of spatial resolution, OSEM performed better than MRP, which in turn performed better than 3DRP.

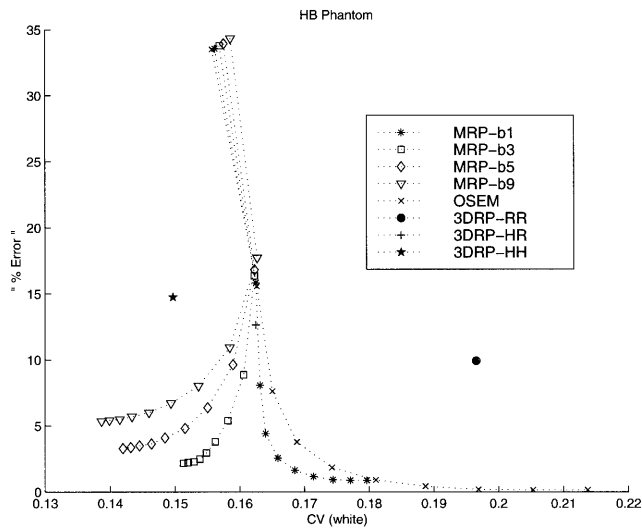


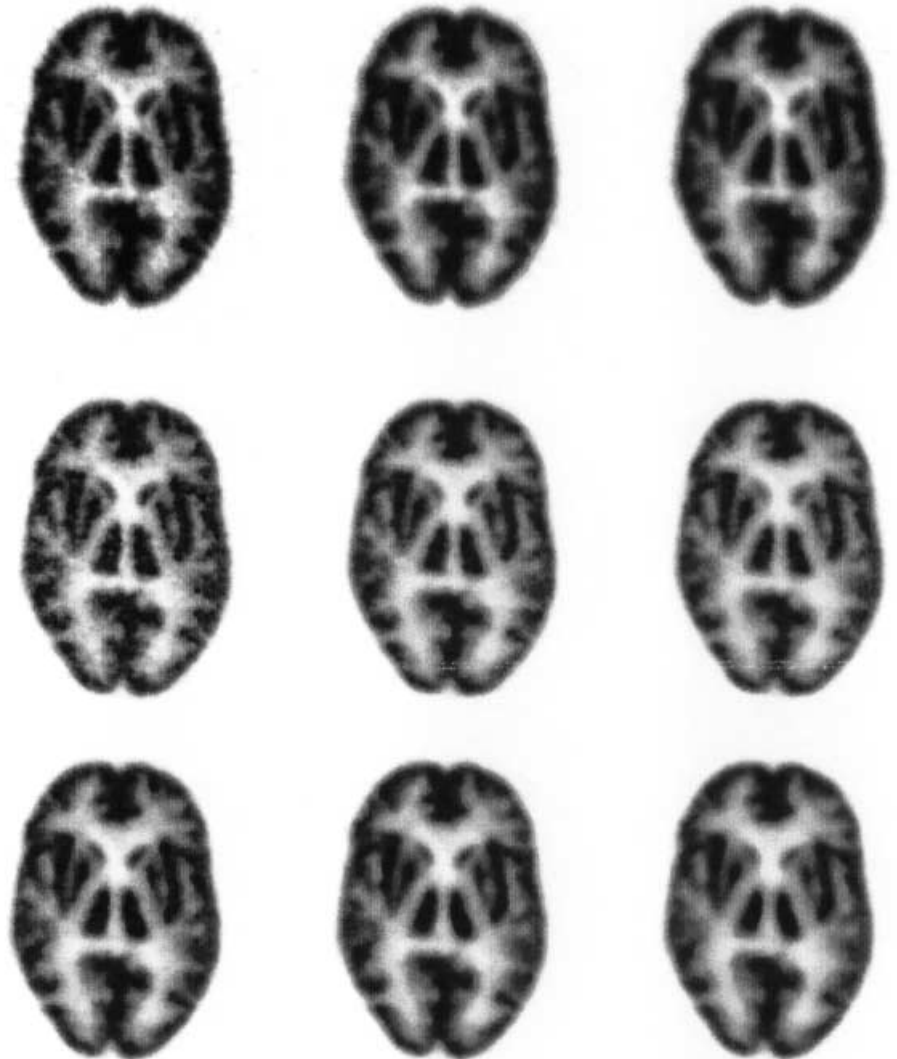
**Fig. 6.** HB phantom. % error of the activity ratio AR between “grey” and “white” matter in relation to the true AR value as a function of CV (calculated for the “white” matter)

## HB phantom

The % errors for the AR with respect to the true value of the “grey/white” matter ratio for the HB phantom are shown in Fig. 6 as a function of CV (calculated over uniform regions of “white” matter). Comparable % error (within 5%) was obtained by OSEM and MRP after 5–6 iterations, while MRP performed better, presenting less noise. For MRP-b3, -b5 and -b9, a noise reduction was observed upon increasing the number of iterations. 3DRP in all reconstruction configurations had a higher % error than iterative algorithms. A representative slice of the phantom reconstructed by the different algorithms is shown in Fig. 7. All images are of “good” quality, showing high contrast between “grey” and “white” matter regions. In particular, good detail preservation is observed in images reconstructed by MRP-b3 and -b5, which are also characterised by low noise.

Figure 8 shows the behaviour of noise (CV in “grey” and “white” matter regions) for MRP reconstructions

**Fig. 7.** HB phantom: image sequence as in Fig. 4



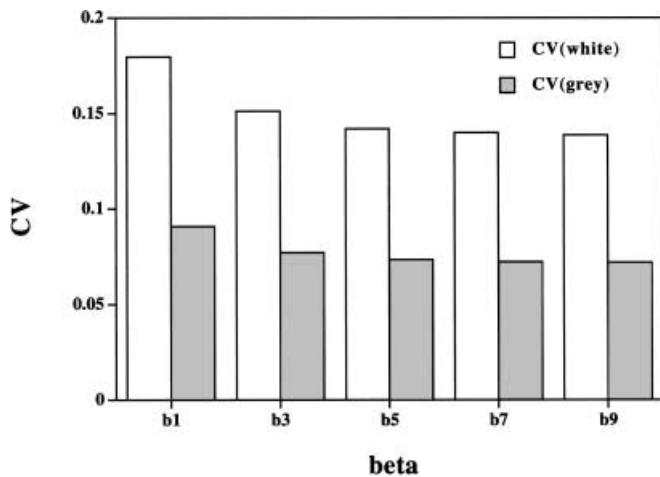


**Fig. 8.** MRP algorithm. CV as a function of  $\beta$  value as calculated for the “grey” and “white” matter of the HB phantom. CV was calculated after 10 complete iterations

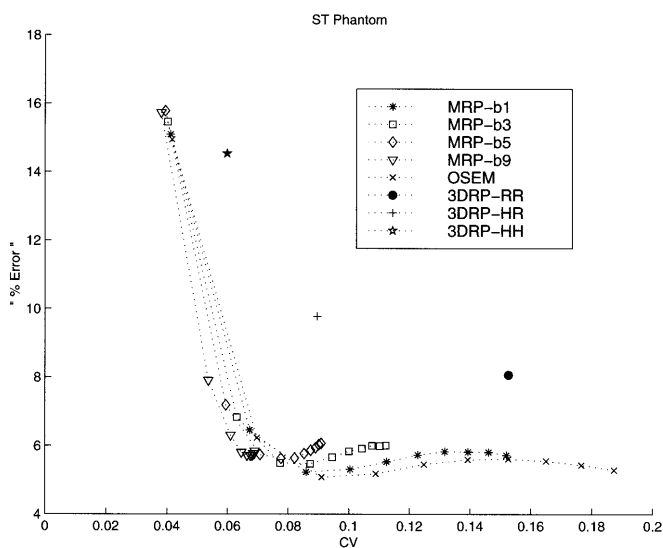


**Fig. 9.** ST phantom. % error of the AR between “putamen” and background in relation to the true AR value as a function of CV (calculated for the background)

(after 10 iterations) as a function of  $\beta$ . CV was consistently lower in “grey” than in “white” matter regions. For both “grey” and “white” matter, CV decreased as  $\beta$  increased, reaching a quite stable value for  $b > b3$ . For  $\beta$  values in the range  $b3$ – $b5$  a good compromise between noise and detail preservation was obtained.

### ST phantom

The % error of AR with respect to the true “putamen”/background AR values for the ST phantom is shown in Fig. 9 as a function of CV (calculated over background regions). MRP and OSEM behaved similarly, reaching a comparable % error (5–6%) after 3–4 com-

plete iterations. 3DRP in all reconstruction configurations resulted in a higher % error than did iterative algorithms. Similar results were found for the “caudate”/background AR values.

In Fig. 10 a representative slice of the ST phantom is shown, reconstructed by the different algorithms. Noise suppression is particularly evident in MRP reconstructed images, without loss of spatial resolution. 3DRP-HH resulted in poor-resolution reconstructed images.

### Clinical data

AR values as a function of CV are reported in Figs. 11 and 12 for the  $^{18}\text{F}$ -FDG and the  $^{18}\text{F}$ -FESP study, respectively. Figures 13 and 14 each show a representative slice of the clinical studies reconstructed by the different algorithms. In both the  $^{18}\text{F}$ -FDG and  $^{18}\text{F}$ -FESP studies, quantitative and qualitative analyses confirmed the results found with the corresponding phantom data (HB and ST phantom).

### Discussion

This paper describes the implementation and evaluation of a one-step late (OSL) maximum a posteriori (MAP) reconstruction algorithm based on the median root prior (MRP) for 3D PET brain studies. The PARAPET ([www.brunel.ac.uk/~masrppet](http://www.brunel.ac.uk/~masrppet)) software package used to develop the algorithm allows implementation of new reconstruction algorithms using standard building blocks (e.g. general image and sinogram manipulation tools, forward- and back-projection routines). The MRP algorithm was evaluated using experimental phantom and clinical 3D PET brain studies. Brain-like phantoms with different radioactivity distribution were considered and PET studies of low and high count statistics were performed to cover a variety of situations.

Data were pre-corrected for randoms, normalisation and scatter while attenuation correction was included in the reconstruction scheme of the iterative algorithms. It is known that including all the physical effects in the reconstruction scheme can improve the quality of the reconstructed images, reducing bias and noise [19, 20, 21, 22, 23]. This should be true particularly in 3D whole-body studies, where heterogeneous and asymmetrical AC maps associated with a very high fraction of scatter (60%–70%) and random events have a significant effect. In brain-like situations, such as those considered in this work (almost uniform and symmetrical attenuation map, with relatively “low” scatter and random fraction), no significant advantage is expected. This was verified in selected studies (data not presented) where fully pre-corrected data showed slightly better contrast and % error but slightly worse CV than when AC was incorporated in the reconstruction scheme. Furthermore the use of



**Fig. 10.** ST Phantom. Image sequence as in Fig. 4

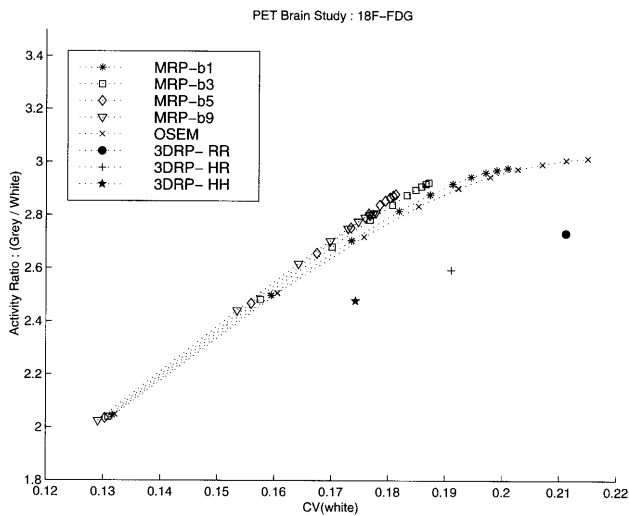


**Fig. 11.**  $^{18}\text{F}$ -FDG brain study. AR between “grey” and “white” matter as a function of CV (calculated for the white matter)

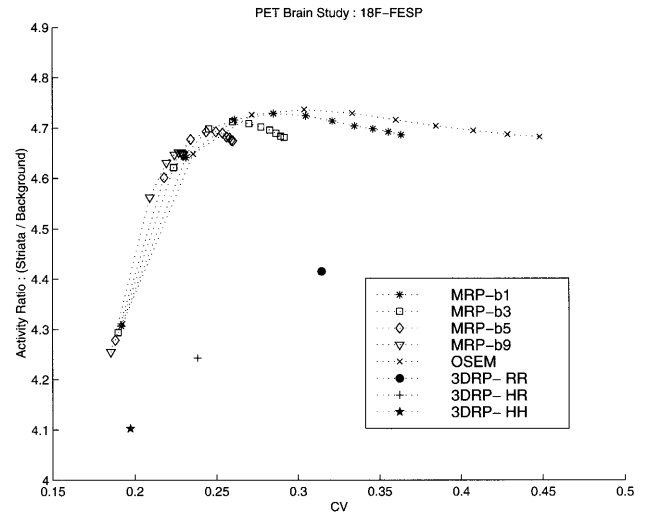
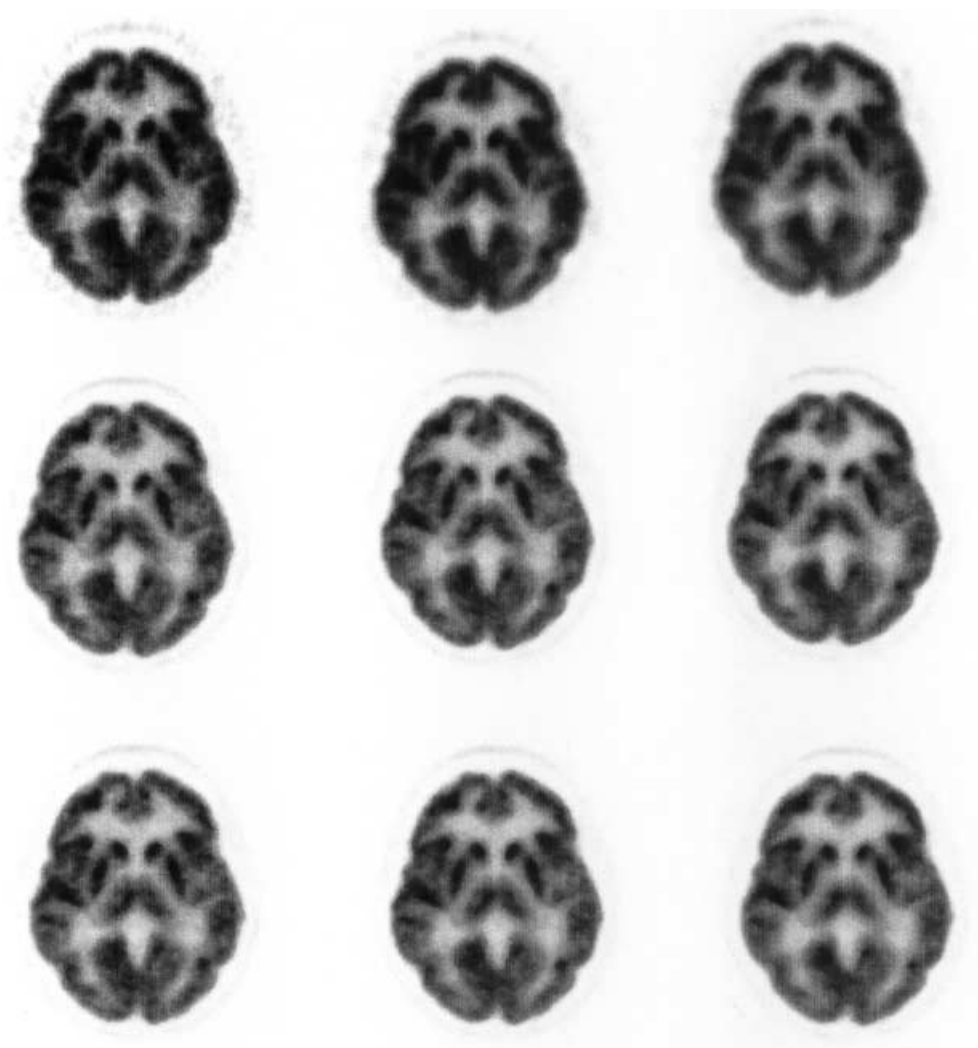


**Fig. 12.**  $^{18}\text{F}$ -FESP brain study. AR between “putamen” and background as a function of CV (calculated for the background)

**Fig. 13.**  $^{18}\text{F}$ -FDG brain study.  
Image sequence as in Fig. 4



partially pre-corrected data simplifies the implementation of the reconstruction algorithms as well as the extraction of the 3D sets of data from the original scanner database. Also, random correction is generally applied on line during the acquisition in order to save disk space, particularly when data are acquired in 3D.

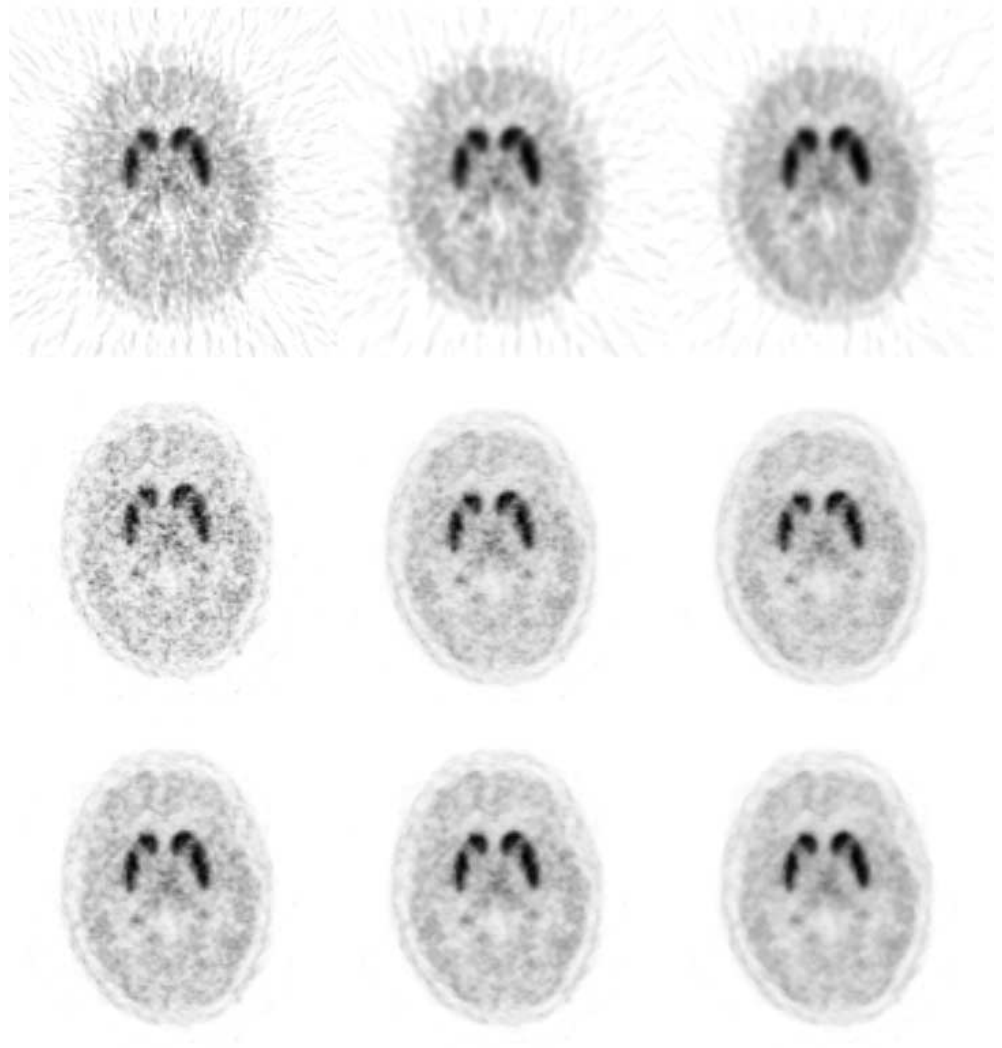
In all the experimental situations considered, MRP showed: (1) convergence or clear trend to a stable solution, (2) effectiveness in noise reduction and (3) preservation of spatial details. The consistency of these observations over different phantoms and radioactivity distributions as well as at high and low counting statistics proves the robustness of the algorithm and suggests its easy optimisation for specific and well-defined tasks.

In fact, the mask width used to calculate the median filter and the weight factor  $\beta$  are the only two parameters involved in an optimisation process of the MRP algorithm. The spatial size of the median mask defines the area over which the criterion of monotonic behaviour is required. This provides the possibility to pre-set the width of the smallest details to be preserved by properly

setting the image dimension, zoom factor (which in this work was equal to 1) and mask width [12].

In this work, the window mask used for the median was applied in 3D as a  $3 \times 3 \times 3$  window. In such a situation, as a result of the median filtering properties, details can be preserved if they cover at least half of the voxels involved during filtration. This consideration can explain the results obtained with the MRP for the 6.4-mm cold rod of the JZA phantom and the 8-mm hot sphere of the MIX phantom, which are, in size, at the lower limit (particularly in the  $z$  direction for the hot sphere) of detail preservation compatible with the parameters set in the MRP reconstructions. Once the mask width has been fixed, a  $\beta$  value has to be set in the algorithm as weight for the prior. The range of  $\beta$  values to be used depends on the values of the PM, which in turn depend on the specific PET system and on the specific attenuation map. In fact there is an order of magnitude (in the case of brain-like sources) between the values of the PM when only geometrical factors are included and the values when geometrical factors and attenuation ef-

**Fig. 14.**  $^{18}\text{F}$ -FESP brain study.  
Image sequence as in Fig. 4



fect are included. A simple empirical means of  $\beta$  selection/optimisation can thus start with a few reconstructions of a representative dataset using different  $\beta$  values covering a wide range of order of magnitude (e.g. 0.5, 0.05, 0.005, 0.0005 and 0.00005). As soon as the best image (qualitatively and quantitatively) is recognised, from among those obtained, the  $\beta$  values can be restricted to a small range on the same order of magnitude. We have shown that  $\beta$  values between 0.0003/subset and 0.0005/subset represent a good compromise in terms of noise reduction and preservation of spatial detail. This can be considered a general result, applicable for all brain-like studies covering a wide range of counting statistics. In this work we used only a 3D median filter and not a 2D median filter in order to avoid the “patchy” appearance typical of the median filters applied in 2D. An alternative solution to this problem was recently proposed by Alenius et al. [24], who suggested substitution of the 2D median filter with a 2D L-FWHM filter to improve the quality of the reconstructed images while maintaining all the other properties of the original MRP formulation.

The performance of the MRP algorithm was compared with that of OSEM and 3DRP, which represent two widely used, fully 3D PET iterative and analytical reconstruction algorithms, respectively. The clinical use of OSEM (for the reconstruction of both 2D and 3D data) generally entails few complete iterations (2–4) and some sort of filtering (intra-iteration or post-reconstruction), in view of the typical increase in noise as the iterations proceed. In this work, the behaviour of OSEM was evaluated at up to 10 complete iterations. In fact, OSEM was not considered as a gold standard for the iterative reconstruction methods, and the comparison between MRP and OSEM was intended to assess the effect of the median penalty on the basic OSEM behaviour. OSEM had better spatial resolution (line source results) than MRP, but MRP was nevertheless effective in preserving spatial detail in both the phantom and the clinical studies. Furthermore, MRP proved able to control the increase in noise (typical of OSEM) in all the experimental situations considered, even for very low count statistics data. Comparison of MRP with the analytical 3DRP algorithm showed that, in general, MRP performs better in terms of

noise reduction and spatial resolution. While comparable results were found for cold spot studies, better performance was obtained with the iterative algorithms in the case of hot spot situations. This is more likely to be due to a “worse” performance of the iterative algorithms in cold spot situations than to a different behaviour of the analytical algorithm in cold and hot spot situations. In fact, to satisfy the positive constraint intrinsic to the iterative algorithms considered, negative numbers in the raw data (due to the pre-correction for randoms and scatter) were set to zero before starting the reconstruction process. Such truncation produces a positive bias, which can eventually result in a reduction in contrast. Furthermore, it is known that OSEM-based algorithms converge more slowly for cold spots than for hot spots. By contrast, hot spot studies are mainly affected by the spatial resolution performance of the algorithms, which was found to be better for iterative algorithms. This could also be observed in the phantom and clinical studies with high activity regions (in particular the ST phantom and  $^{18}\text{F}$ -FESP studies), where the transaxial and axial filtering applied by  $3\text{DRP}_{\text{HR}}$  and  $3\text{DRP}_{\text{HH}}$  reduced the noise but at the expense of loss of spatial resolution.

In conclusion, MRP represents a very effective and promising reconstruction algorithm for 3D PET brain data, in particular owing to its simplicity in terms of the penalty used, which naturally reduces the noise, and its robustness in different and complex experimental situations.

## References

- Shepp L, Vardi Y. Maximum likelihood reconstruction for emission tomography. *IEEE Trans Med Imag* 1982; 1:113–122.
- Lange K, Carson R. EM reconstruction algorithms for emission and transmission tomography. *J Comput Assist Tomogr* 1984; 8:306–316.
- Kaufman L. Implementing and accelerating the EM algorithm for positron emission tomography. *IEEE Trans Med Imag* 1987; 6:37–51.
- Hudson H, Larkin R. Accelerated image reconstruction using ordered subsets of projection data. *IEEE Trans Med Imag* 1994; 13:601–609.
- Biemond J, Lagendijk R, Mersereau R. Iterative methods for image deblurring. *Proc. IEEE* 1990; 78:856–883.
- Veklerov E, Llacer J. Stopping rule for the MLE algorithm based on statistical hypothesis testing. *IEEE Trans Med Imag* 1987; 6:313–319.
- Snyder D, Miller M, Thomas T, Polite D. Noise and edge artifacts in maximum likelihood reconstructions for ET. *IEEE Trans Med Imag* 1987; 6:228–238.
- Llacer J, Veklerov E, Coakley K, Hoffman E, Nunez J. Statistical analysis of maximum likelihood estimator images of human brain FDG PET studies. *IEEE Trans Med Imag* 1993; 12:215–231.
- Green P. Bayesian reconstructions from emission tomography data using a modified EM algorithm. *IEEE Trans Med Imag* 1990; 9:84–93.
- Lange K. Convergence of EM image reconstruction algorithms with Gibbs smoothing. *IEEE Trans Nucl Sci* 1992; 39:1454–1459.
- Bouman C, Sauer K. A generalized Gaussian image model for edge preserving MAP estimation. *IEEE Trans Imag Proc* 1996; 5:480–492.
- Alenius S. On noise reduction in iterative image reconstruction algorithms for positron emission tomography. PhD Thesis. Tampere University of Technology, Pub.265.
- Alenius S, Ruotsalainen U, Astola J. Attenuation correction for PET using count-limited transmission images reconstructed with median root prior. *IEEE Trans Nucl Sci* 1999; 46:646–651.
- Seret A. Median root prior and ordered subsets in Bayesian image reconstruction of single photon emission tomography. *Eur J Nucl Med* 1998; 25:215–219.
- Labbé C, Thielemans K, Zaidi H, Morel C. An object oriented library incorporating efficient projection/back projection operators for volume reconstruction in 3D PET. *IEEE Proc. Int. Meeting on Fully Three-Dimensional Image Reconstruction in Radiology and Nuclear Medicine*. 1999:137–140.
- Kinahan PE, Rogers JG. Analytic 3D image reconstruction using all detected events. *IEEE Trans Nucl Sci* 1989; 36:964–968.
- Jacobson M, Levkovitz R, Ben Tal A, Thielemans K, Spinks T, Belluzzo D, Pagani E, Bettinardi V, Gilardi MC, Mitra G, Zverovich A. Enhanced 3D PET OSEM reconstruction using inter-update Metz filtering. *Phys Med Biol* 2000; 45:2417–2439.
- Bettinardi V, Pagani E, Gilardi MC, Landoni C, Riddell C, Rizzo G, Castiglioni I, Belluzzo D, Lucignani G, Schubert S, Fazio F. An Automatic classification technique for attenuation correction in positron emission tomography. *Eur J Nucl Med* 1999; 26:447–458.
- Polite DG, Snyder DL. Corrections for accidental coincidences and attenuation in maximum-likelihood image reconstruction for positron emission tomography. *IEEE Trans Med Imag* 1991; 10:82–89.
- Carson RE, Yan Y, Chidkowski BA, Yap TK, Daube-Witherspoon ME. Precision and accuracy of regional radioactivity quantitation using the maximum likelihood EM reconstruction algorithm. *IEEE Trans Med Imag* 1994; 13:526–537.
- Qi J, Leahy RM, Hsy C, Farquhar TH, Cherry SR. Fully 3D Bayesian image reconstruction for the ECAT EXACT HR+. *IEEE Trans Nucl Sci* 1998; 45:1096–1103.
- Yavuz M, Fessler J. Penalized Likelihood estimator and noise analysis for randoms precorrected PET transmission scans. *IEEE Trans Med Imag* 1999; 18:1–10.
- Michel C, Sibomana M, Bol A, Bernard X, Lonnet M, Defrise M, Comtat C, Kinahan PE, Townsend DW. Preserving Poisson characteristics of PET data with weighted OSEM reconstruction. *IEEE MIC conference*. 1998:record M6–61.
- Alenius S, Ruotsalainen U. Improving the visual quality of median root prior images in PET and SPECT reconstruction. *IEEE NSS and MIC conference*. 2000:record 386.